RSC Advances

ROYAL SOCIETY OF CHEMISTRY

www.rsc.org/advances

Nanostructuring of Nanoporous Iron Carbide Spheres *via* Thermal Degradation of Triple-shelled Prussian Blue Hollow Spheres for Oxygen Reduction Reaction

Mohamed B. Zakaria[1,2,3]*

[1] *Faculty of Science and Engineering, Waseda University, 3-4-1 Okubo, Shinjuku, Tokyo, 169-8555, Japan.*

[2] *World Premier International (WPI) Research Center for Materials Nanoarchitechtonics (MANA), National Institute for Materials Science (NIMS), 1-1 Namiki, Tsukuba, Ibaraki 305-0044, Japan.*

[3] *Department of Chemistry, Faculty of Science, Tanta University, Tanta (31527), Egypt.*

*E-mail: MOHAMED.Barakat@nims.go.jp or mbarakat14@akane.waseda.jp

Abstract

A template free strategy for designing hollow Prussian Blue (PB) spheres with multi-shells is reported here. Small PB seeds were synthesized under optimized conditions using polyvinylpyrrolidone as a controlling agent. The large crystals grow from the smaller ones which have higher solubility. Voids gradually grow in the core of the large aggregates and the shell thickness increases owing to the outward diffusion of the solutes through the permeable shell leading to core-shell structure. Many shells could form at the surface of the core-shell structure through a step-by-step epitaxial crystal growth. A subsequent etching leads to the formation of triple-shelled PB hollow spheres. A controlled thermal treatment under nitrogen yielded nanoporous iron carbide hollow spheres. The morphology is well-retained after the thermal treatments at 450 °C and completely destroyed at 700 °C because of the crystallization of the metal framework and the fusion of the pores. Nanoporous iron carbide demonstrates an efficient electrocatalytic activity for the oxygen reduction reaction. It shows a better durability than the commercial PtC-5% catalyst, with only 8% loss of the current density during the first 3500 s.

Keywords: Prussian blue; Ostwald ripening; etching; hollow spheres; multi-shells; retention; nanoporous iron carbide; ORR.

Introduction

Inorganic hollow spheres with nanometer dimensions and multiple microporous thin shells can be widely applied in catalysis, drug delivery, energy conversion and storage systems, chemical sensors, biotechnology, etc.[1] In order to meet the requirements of the rapid development of the prementioned applications, recent research efforts have aimed at designing hollow spheres with defined composition and an elaborated inner structure (*e.g.,* multi-shelled hollow structures) to ultimately provide an improved performance in drug release with prolonged release time, heterogeneous catalysis, and Li-ion batteries.[2] The current synthetic methods are only suitable for the synthesis of single-shelled hollow spheres made of a single phase. Therefore, finding facile routes for producing multi-shelled hollow spheres with sophisticated nanostructures of any desired material remains a significant challenge.

The two existing approaches for preparing hollow inorganic materials can be summarized as the hard- and soft-templating methods.[3] The hard-templating route is useful for preparing hollow particles with highly crystallized frameworks and nanodimensional porous structure, but it has several practical drawbacks. Large amount of the solvents are necessary to dissolve the targeted inorganic templates after introducing the metal sources into the templates. In some cases, harmful HF solution is needed if the template is made of mesoporous silica or zeolitic materials. It remains difficult to print the porous structure after removal of mesoporous silica/carbon/polymer matrix by treating with corrosive HF or by calcination in aerobic environment. The porous inorganic structure is likely to collapse and destroy easily in both cases. In case of the soft-templating route, the formation of hollow structures can be inconvenient as it requires various structure directing agents (*e.g.,* surfactants, block copolymers, etc.) and the removal of the template while maintaining the structure intact is still a challenge.[4]

A promising approach for preparing hollow spheres with multi-shells is the template-free strategy which permits to avoid the limitations of the soft- and hard-templating methods. Recently, the Ostwald ripening method has been proposed as a template-free strategy and can be employed for the fabrication of inorganic hollow spheres and dendritic structures.[5] The large crystals grow from the smaller ones which have a higher solubility. Within a colloidal aggregate, small or ‘soft’ crystallites dissolve

into the liquid phase and participate to the growth of larger or 'hard' crystals. Once the particles with different sizes are attached to each other, the large particles begin to grow out from the smaller ones. Voids gradually form and grow in the core of large aggregates, and the shell thickness increases owing to the outward diffusion of the solutes through the permeable shell.[5a] The treatments of these large particles with specific solvents leads to the formation of fine hollow nanoparticles with shells containing micro- and/or mesopores.

Porous coordination polymers (PCPs) and metal-organic frameworks (MOFs) constitute an interdisciplinary field originating from inorganic and coordination chemistry. It has expanded rapidly in the last two decades and is attracting the interest of the chemical engineering.[6-10] The developments of these materials is assessed in terms of the investigations of their property and the enhancements in different disciplines such as catalysis, conductivity, magnetism, optics, sensors, storage, separation, and porosity.[11-17] In the recent years, PCPs have been given much attention, from both scientific and commercial perspectives due to their great potential in many applications. They can be used as advanced catalysts and drug carriers because of the regularity of their pore shape and size as well as their functionalities.[18-20]

Several works have been achieved to design hollow PCPs with multiple thin shells to increase their surface area and consequently improve their physical properties. So far, controlling the preparation of sophisticated hollow PCPs has been successfully achieved, leading to advanced materials that can bring out new properties and be utilized to solve problems related to the energy and the environment.[21-25] For example, the synthesis and characterization of organometallic CPs nanoshells of PB using miniemulsion periphery polymerization (MEPP) and self-assembly of stable nanoscale coordination polymers (NCPs) were previously reported.[26-30] Moreover, hollow ferrocenyl CPs microspheres with microporous shells were synthesized.[31-32] In these procedures, the conjunction of porous ZIF-8 with polystyrene spheres induces the formation of polystyrene@ZIF-8 structures. The subsequent etching process removes the polystyrene cores, leading to a unique hollow ZIF-8. Furthermore, McHale *et al.* reported PB coordination polymer nanobox synthesized using MEPP.[33] Suping *et al.* have succeeded to synthesize and characterize ultrathin metal coordination PB nanoribbons.[34]

In this contribution, we report a promising method for designing and synthesizing

triple-shelled PB hollow spheres (*i.e.,* $Fe_4[Fe(CN)_6]_3 \cdot xH_2O$) through a step-by-step crystal growth and a subsequent selective chemical etching. Many shells were developed into small PB seeds by epitaxial crystal growth. In the light of the Ostwald ripening concept, it has been generally known that the PB colloidal nanocubes are formed by self-aggregation of small nanocrystals that lead to defects within the nanocubes. The distribution of the defects varies by different locations owing to the in-uniform fusion of the nanocrystals. The dissolution and recrystallization can help to reduce the defects/voids in the shell. Therefore, specific defects distribution can be expected inside the PB colloidal nanocubes. For each nanocube, the inner region has more defects than the outer surface, similar to a core-shell structure. Many shells can be developed into the core-shell structure leading to solid PB nanocubes with multi-shells. After etching the PB nanocubes using diluted hydrochloric acid, hollow PB spheres with multi-shells and a large inner cavity were successfully obtained.

Moreover, we have reported the thermal decomposition in air of hollow and solid PB nanocubes.[35] In general, this reaction is accompanied by the loss of water molecules in the early stage of the heating treatment followed by the subsequent release of gaseous $(CN)_2$ or HCN products. In the meantime, oxidation of iron cations leads to the formation of iron oxide as a common decomposition product. The obtained Mössbauer parameters were assigned to α-Fe_2O_3 in case of the calcined hollow PB nanoparticles and was used as a photocatalyst for the degradation of methylene blue.[35a] Otherwise, according to the XRD data and the measured magnetic properties γ-Fe_2O_3 was attributed in case of the calcined solid and showed a great potential as drug delivery vehicles with high biocompatibility, controlled release of bladder cancer cells (*i.e.,* T24), and magnetic targeting features for future intracellular drug delivery system.[35b] From the results, we conclude that the hollow structure has a critical effect on the final iron oxide product. Likewise, the thermal decomposition of hexacyanoferrate compounds in vacuum at lower temperatures was also reported.[36] The authors concluded that the structure of the solid PB particles heated in vacuum at temperature lower than 400 °C was partially decomposed and exhibited mixed-valence states. Therefore, herein we study the thermal decomposition of hollow PB spheres under nitrogen at temperatures higher than 400 °C to complete the general understanding of the thermal behavior of PB and its ability to retain its morphology in the air or under nitrogen. To our knowledge,

the thermal decomposition of hollow PB spheres under nitrogen has never been reported before.

Experimental section

Chemicals

Polyvinylpyrrolidone (PVP, K30) was purchased from Nacalai Tesque, Japan. Potassium hexacyanoferrate (III) ($K_3[Fe(CN)_6]$) was purchased from Merck KGaA, Germany. Hydrochloric acid (HCl) and potassium hydroxide (KOH) were purchased from Wako, Ltd, Japan. Nafion® perfluorinated resin solution 5 wt.% was purchased from Sigma-Aldrich, USA. All chemicals were used without further purification.

Synthesis of Triple-Shelled PB Solid Nanocubes (BD^3NC)

In a typical procedure, double-shelled PB solid nanocubes were simply synthesized following a wet-chemical method previously reported by Hu *et al.*[37] Then, a third shell was developed by us for the synthesis of BD^3NC. The details are as follow: PVP (6.00 g) and $K_3[Fe(CN)_6]$ (264 mg) were added to a 0.1 M HCl solution (80.0 mL) under constant magnetic stirring. After 30 min, a clear yellow solution was observed. The vial was then placed into an electric oven and heated at 80 °C for 18 h. Following this aging process, the resulting blue precipitate was collected by centrifugation and washed several times with distilled water and ethanol. After drying at room temperature for 24 h, a blue powder was obtained and used as seeds for the next step. This full synthesis process is referred as the PB growth.

The seeds (20.0 mg), PVP (6.00 g), and $K_3[Fe(CN)_6]$ (264 mg) were then added to a 0.01 M HCl solution (80 mL) under magnetic stirring and the whole PB growth process was repeated. Bright and dense PB nanocubes with an average particle size of ~200 nm, referred as BDNC, were obtained after the first round. PB nanocubes with an average particles size of ~300 nm, referred as BD^2NC, were obtained after the second round. Finally, PB nanocubes with an average particles size of ~420 nm, referred as BD^3NC, were obtained after the last round. The used amount of $K_3[Fe(CN)_6]$ for the last round is 396 mg.

Conversion of BD^{3}NC into Triple-Shelled PB Hollow Spheres (TPBHS)

The obtained BD^{3}NC (160 mg) were immersed in 160 mL of 1 M HCl solution in a Teflon vessel under magnetic stirring. After sonication for 10 min and a subsequent stirring for 30 min, the vessel was transferred into a stainless autoclave and heated at 135 °C for 3.5 h in an electric oven (Caution! The −C≡N− groups may be converted into HCN gas in hot acidic solution. The process should be carried out in a fume hood). After cooling, the precipitate was collected by centrifugation and washed in distilled water and ethanol several times. After drying at room temperature for 24 h, TPBHS could be obtained.

Conversion of TPBHS into Nanoporous Iron Carbide (NIC)

The obtained TPBHS were used as a precursor for thermal conversion into NIC. The powder (100 mg) was placed inside a melting pot which was then heated inside an electronic furnace oven with a heating rate of 5 °C min^{-1} up to a desired temperatures (450 °C, 550 °C, and 700 °C) and kept annealing for 1 h in order to remove the nitrogen atoms completely. Then, the powder was cooled inside the furnace with at the same rate. Finally, the obtained black powder was collected for characterization. All calcination process was carried out under nitrogen with a flow rate of 120 mL min^{-1}.

Electrochemical Measurements

For electrode preparation, a rotating disk electrode (RDE) was first polished using alumina suspensions with decreasing particle size (*i.e.,* typically from 1.0 to 0.05 μm). The polishing should be in a circle motion. It is critical to rinse carefully the surface of the electrode with water between every polishing step, followed by drying under nitrogen flow. The as-prepared catalyst (5 mg) was mixed with 950 μL of mixed water-ethanol solution (3:1 ratio) under sonication until it becomes homogeneous. Then, 50 μL of nafion perfluorinated resin solution was added to the suspension. After sonication for 15 min, 5 μL of the homogeneous suspension was deposited at the center of the top surface of the electrode and left to dry for 2 h.

Electrochemical Analysis Techniques

Cyclic voltammograms (CVs) and linear sweep voltammetric (LSV) curves were

achieved with a CHI 842B electrochemical analyzer (CH Instrument, USA). A conventional three-electrode cell was used, including an Ag/AgCl electrode as a reference electrode, a platinum wire or a graphite rode as a counter electrode, and a glassy carbon rotating disk electrode (RDE) modified with the catalyst as a working electrode. Before the RDE experiments, the aqueous 0.1 M KOH electrolyte was bubbled with oxygen for at least 1 h.

Characterization

Scanning electron microscope (SEM) images were taken with a Hitachi SU8000 at an accelerating voltage of 5 kV. The transmission electron microscope (TEM) observations were performed using a JEM-2100F TEM system operated at 200 kV and equipped for energy-dispersive spectrometer analysis. Wide-angle powder x-ray diffraction (XRD) patterns were obtained with a Rigaku RINT 2500X diffractometer using a monochromated Cu Kα radiation (40 kV, 40 mA) at a scanning rate of 2 ° min^{-1}. X-ray photoelectron spectroscopy (XPS) spectra were recorded at room temperature using a JPS-9010TR (JEOL) instrument with an MgKa X-ray source. All binding energies were calibrated by referencing to C 1 s (285.0 eV). Nitrogen gas adsorption-desorption isotherms were obtained with a Quantachrome Autosorb Automated Gas Sorption System at 77 K. Fourier Transform Infrared Spectroscopy (FTIR) spectra were collected using a Thermoscientific Nicolet 4700 in a transmission mode.

Results and discussions

The schematic illustration of the design and synthesis of TPBHS and its thermal conversion into NIC is outlined in Figure 1. First small PB seeds were synthesized, rearranged, aggregated, and fused to from core-shell structure. Then, three outer PB thin shells were developed into the core-shell structure leading to BD^3NC which converted into TPBHS by etching. A controlled thermal treatment under nitrogen yielded NIC spheres.

The surface morphology of the prepared solid and hollow PB nanoparticles was examined by using SEM, as shown in Figure 2. The starting PB crystals seeds with approximately 90 nm in size were synthesized under controlled crystal growth

conditions with the assistance of PVP (Figure 2a). PVP mainly serves as a capping or chelating agent that stabilizes the nucleus at first. In the case of low concentrations of PVP, the particles directly precipitate without further crystal growth. On the other hand, if the amount of PVP is sufficient, the nucleus can stabilize and self-assemble in an ordered manner.[38] Larger PB nanocubes (~200 nm) were grown onto the surface of the starting seeds (Figure 2b). It has been generally known that the PB colloidal nanocubes are formed by self-aggregation of smaller nanocrystals that leads to defects within the larger structures. The defects distributions were characterized from the stair-like edges and corners of the nanocubes clearly observed from the SEM images. During etching these defects/voids permit acid enter inside the nanocubes to create holes and works also in the intermediate surface between the shells. The distribution of the defects varies by different locations owing to the in-uniform fusion of tiny nanocrystals. The dissolution and recrystallization can reduce the defects in the shell region. Therefore, the defects are specifically located inside the PB colloidal nanocubes, thus forming a core-shell structure. The core region rich in defects is labelled as "bright" (B), while the shell region is labelled as "dense" (D). Thus, the whole bright and dense nanocubes are further referred as BDNC. The BDNC was utilized as seeds for the growth of another layer of PB into its surface. The additional layer also has a BDNC structure, thus leading to a BD^2NC fused nanoparticles (~300 nm), as shown in Figure 2c. Triple-shelled BD^3NC (~420 nm) was further obtained by growing a third PB layer on the BD^2NC (Figure 2d). When these particles are immersed in an acidic solution, H^+ ions can pass through the defects/voids and spaces from the shells and react inside the particles. Because of the non-uniform distribution of the defects, the etching rate varies accordingly. The regions with more defects are indeed etched more quickly. Therefore, the "bright" regions were removed, while the "dense" regions were preserved, resulting in TPBHS with micro- and mesopores (Figure 2e). The creation of holes inside the nanocubes and formation of multi-shells can be used for characterization of the distribution of defects. Moreover, the distribution of Fe atoms was confirmed by the elemental mapping (Figure 2f). The core and the space between shells seem to be more bright indicating the succeefully formed TPBHS and homogeneous distribution of Fe atoms over the top surface.

It is well-known that PB is composed of iron ions with mixed valences (*i.e.,* Fe^{2+} and

Fe^{3+}) combined with a framework in which cyanide-groups act as bridges (-Fe^{II}-C≡N-Fe^{III}-).[30a] To understand the electric states of Fe atoms, the obtained TPBHS were examined by XPS analysis (Figure S1). The Fe $2p_{3/2}$ can be divided in two contributions (708.3 and 712.8 eV) which can be assigned to the Fe^{2+} of $[Fe(CN)_6]^{4-}$ and Fe^{3+} oxidation states.[30b] The calculated molar ration of Fe^{3+}/Fe^{2+} is around 4/3, which is in accordance with the theoretical value.[3a] Moreover, The sharp peaks observed by wide-angle XRD (Figure S2a) revealed that the as-synthesized TPBHS adopt a highly crystallized face-centered cubic (*Fm-3m*) structure compared to the PB crystals (JCPDS card no. 73-0687).[30a] This evidences that the etching process led to particles with an inner cavity while maintaining the original structural integrity. No extra peaks derived from impurities were detected, suggesting that the product has a high purity.

Nitrogen gas sorption isotherms are performed in order to calculate the structure parameters and to examine the nanoporous characters of TPBHS, as shown in Figure S2b. The increase at low relative pressure ($P/P_0 < 0.1$) indicates the presence of inherent micropores in the shells of TPBHS. Between 0.1 and 0.4, a large amount of N_2 is adsorbed, reflecting the abundant macropores contained in TPBHS, formed during the etching process (inset in Figure S2b). This is consistent with the mesopores in the shell region observed on SEM image (Figure 2e). Their sizes have a wide distributed distribution, ranging from a few nanometers to ~38 nm. Because of the additional mesoporosity, the calculated surface area is 250 m^2 g^{-1} and a large hysteresis loop can be observed.

TEM and electron diffraction (ED) images of the BD^3NC solid nanocubes are presented in Figure 3a. The presence of stair-like edges suggest the large nanocubes are formed from aggregates of smaller crystals and the periodic diffraction spots taken from the edge of a single cube (inset in Figure 3a) indicate that the monocrystalline particles have a common orientation. The contrast between the darker shells and brighter cores is an evidence of the BD^3NC structure. BD^3NC are then dispersed in a hot diluted HCl solution and underwent etching. Figure 3b shows a clear image of the internal structure of TPBHS with fine morphology. One can clearly observe three concentric layers along with the cavity. Interestingly, the outer and inner layers share the same crystallographic orientation, as suggested by the ED patterns (inset in Figure 3b). A low magnification

TEM images (Figure 3c) was inserted o assess the homogeneity of TPBHS. Few small particles are formed because of the deterioration of some large particles during heating but they are negligible. High-angle annular dark field scanning transmission electron microscope (HAADF-STEM) was employed to further confirm the successful synthesis of the TPBHS. A quasi-cubic shape with highly symmetric curved edges was observed (Figure 3d).

The thermal conversion of PB into iron carbide is a promising application. Upon heating under nitrogen or vacuum at lower temperatures (*i.e.,* < 200 °C), the entrapped water molecules can be easily removed,[39] while heating at higher temperatures (*i.e.,* > 400 °C) leads to formation of polymorphs of iron carbide. These include orthorhombic Fe_2C as well as some impurities such as graphite, free carbon and metallic iron. By further increasing the temperature, metallic iron can be obtained as a main product.[39] Thus, TPBHS were thermally treated at 450 °C, 550 °C, and 700 °C under nitrogen for 1h. It can be seen from the SEM images (Figure 4a) that the iron carbide formed at 450 °C retained the nanoporous spheres (~270 nm) structure. By increasing the temperature up to 550 °C, some of the spheres tend to collapse and shrink and the average particle size increases due to an outward diffusion of iron ions during the thermal treatment (Figure 4b). If the temperature is further increased up to 700 °C, all the spheres entirely collapse because of the complete crystallization of the iron frameworks (Figure 4c).

The FTIR spectra confirm the complete conversion of TPBHS into NIC, as shown in Figure 4d. TPBHS return a typical fingerprint spectrum of PB, with a peak at 2110 cm^{-1} attributed to the CN stretching in the formed $–Fe^{II}–CN–Fe^{III}–$ structure, an absorption band at 494 cm^{-1} due to $Fe^{3+}–CN$ formation (considered to be the main source of PB crystals), and absorption bands at 1610 cm^{-1} and 3415 cm^{-1} corresponding to the bending mode of H–O–H and stretching mode of O–H, respectively.[40] The disappearance of the CN band and other characteristic bands of PB after heating at 450 °C suggests a complete conversion into iron carbide. This result correlates with the XRD patterns (Figure 5a). The patterns can be assigned to an orthorhombic Fe_2C as a main product (PDF card no. 03-065-1456).[39] Some peaks corresponding to graphite, free carbon,[41] and metallic iron[39] are also present. Surprisingly, after heating at elevated temperatures (*i.e.,* 550 and 700 °C), an absorption band at 633 cm^{-1} was observed in the

FTIR spectra, which is characteristic to Fe–O. Moreover, according to XRD patterns (Figure 5b), the peaks corresponding to metallic iron and graphite are sharper and more intense after annealing at 700 °C. These results, combined with the SEM images from Figures 4b and 4c, suggest that heating at elevated temperature is not favorable for retaining the spherical morphology of the iron carbide particles.

To investigate the porosity of the obtained NIC, nitrogen gas adsorption-desorption isotherms measurements were performed (Figure 6a). The average pore volume (0.359 cm^3 g^{-1}) and diameter (4.19 nm) were calculated using the Barrett-Joyner-Halenda (BJH) method. The calculated surface area (BET) was 89.97 m^2 g^{-1}. From the isotherms, the shape is almost similar to a type IV isotherm with a hysteresis loop, according to IUPAC classification, which is associated to capillary condensation taking place in the mesopores. When this process occurs at high relative pressure, this indicates a larger pore-size distribution (inset in Figure 6a). This may be attributed to the fusion of micropores into lagers pores after heating, even though the obtained size distribution corresponds mainly to mesopores.[41] NIC was further characterized by TEM and ED. As shown in Figure 6b, the shells are decorated with plentiful and dense pores. The final morphology is well retained even after heating. When compared with the PB spheres, the average particles size is slightly decreased (~270 nm). The intense oriented spots arranged in a circular shape, observed in the ED pattern (inset in Figure 6b), are characteristic of polycrystalline grains.

Inspired by the unique structure of NIC, the oxygen reduction reaction (ORR) was selected as a target reaction to ascertain their potential implementation in energy conversion systems. First, cyclic voltammetric (CV) measurements were carried out in 0.1 M KOH saturated with N_2 and O_2 to determine the oxygen reduction activity of the obtained sample. By comparing the CV curves (with N_2 and O_2), it was confirmed that our material shows a significantly enhanced catalytic ORR activity in O_2-saturated alkaline solution (Figure 7a). Specifically, an ORR onset potential of about -200 mV *vs.* Ag/AgCl and peak current at about -400 mV were observed. It is expected that small molecule-based organic fuels (such as methanol) can penetrate through a polymer electrolyte membrane from the anode to the cathode easily and subsequently compromise the whole cell performance.[42] Our material could effectively avoid such crossover effect in comparison to the Pt-based materials when used directly in methanol

fuel cells.

The oxygen reduction reaction performance of NIC was further tested by using a rotating disk electrode (RDE) in an O_2-saturated 0.1 M KOH solution at a rotation speed of 1600 rpm and a scan rate of 10 mV s^{-1}. The linear sweep voltammograms (LSVs) was shown in Figure 7b. The influence of NIC on the behavior toward the ORR was confirmed from the polar curves. The onset potential for the oxygen reduction reaction on NIC is around -200 mV *vs.* Ag/AgCl in the scan range from 0 to -1000 mV. All the results indicate that our material is responsible for the ORR activity. Finally, NIC may decrease the mass transport resistance and allow the access of the electrolyte to the active surface sites easier, which is greatly beneficial for the ORR process.[43] In addition, the stability of the catalysts is another factor should be well considered in the usage of the catalysts. Therefore, a chronoamperometric measurement in a time period of 3500 s was further checked for our material. The current retention performance was recorded in Figure 7c. It is obvious that NIC shows a current loss of only 8% and high current retention efficiency (*i.e.,* 92%). After comparison, it shows much better durability than the commercial PtC-5% catalyst

The electron transfer number (n) involved in NIC for the catalytic ORR was estimated to be 3.55 from the rotating ring-disk electrode plot (RRDE; Figure 7d). To obtain in-depth understanding on the ORR process, RRDE voltammograms were measured. The corresponding amperometric current (upper curve) for the oxidation of hydrogen peroxide ions (HO_2^-) was recorded at the Pt ring electrode, which is effective to monitor the formation of intermediate peroxide species. Specifically, the calculated peroxide yield was 23 % at a potential of 0.5 V *vs.* Ag/AgCl. The electron transfer number per oxygen molecule involved in the ORR was calculated from RRDE voltammograms according to the following equation.[43]

$$n=4\times I_d / (I_d+I_r/N) \quad (1)$$

Where; I_d is the disk current, I_r is the ring current and N = 0.37 is the collection efficiency of Pt ring.

Meanwhile, the peroxide percentage ($\%OH_2^-$) was calculated based on the following equation.[44a]

$$\%OH_2^- = 200(I_r/N) / (I_d+I_r/N) \quad (2)$$

In order to gain insight to the kinetics of ORR on our iron carbide hollow spheres, we

conducted the RDE measurements under different rotation speeds from 400 rpm to 2500 rpm with a scan rate of 10 mV s^{-1}. The polarization curves are shown in Figure S3a. The corresponding Koutecky-Levich plot (J^1 vs. $\omega^{-1/2}$) for iron carbide showed good linearity, indicating the first-order reaction kinetics with respect to the oxygen concentration and constant electron transfer numbers for oxygen reduction reaction at a potential of -0.5 V *vs.* Ag/AgCl (Figure S3b). The kinetic parameters can be analyzed on the basis of the following Koutecky-Levich equations.[45]

$$J^{-1} = J_L^{-1} + J_K^{-1} = B^{-1}\omega^{-1/2} + J_K^{-1} \quad (3)$$

$$B = 0.62nFC_0(D_0)^{2/3}\nu^{-1/6} \quad (4)$$

Where; J is the measured current density, J_K and J_L are the kinetic- and diffusion-limiting current densities, ω is the angular velocity of the disk, n represent the overall number of electrons transferred in oxygen reduction, F (C mol^{-1}) is the Faraday constant, C_0 (mol L^{-1}) is the bulk concentration of O_2, ν (cm^2 s^{-1}) is the kinematic viscosity of the electrolyte, D_0 (cm^2 s^{-1}) is the diffusion coefficient, and k is the electron transfer rate constant. The number of electrons transferred (n) can be obtained from the slope of the Koutecky-Levich plots. The transferred electron number (n) was estimated to be 3.5 for the iron carbide electrode. The overall results indicate that the ORR using ICHS involves mainly four-electron reaction.

Other counter electrodes were reported (*e.g.,* Ni sheet and graphite rode) to avoid the contamination of the working electrode by Pt.[46] Thus, for confirmation, we checked the electrochemical activity of NIC again for ORR using a graphite rode as a counter electrode instead of Pt-wire (Figure 8). Comparison of the cyclic voltammetric curves of the sample examined in 0.1 M KOH saturated with N_2 and O_2 confirmed that our material shows a significant enhancement of ORR activity in O_2-saturated alkaline solution (Figure 8a). An improvement in the activity in case of O_2-saturated alkaline solution was observed. The ORR onset potential is at around -200 mV *vs.* Ag/AgCl and a peak current was shifted to be noticed at a lower potential (-370 mV). The linear sweep voltammograms at different rotation speeds and a constant scan rate of 10 mV s^{-1} were shown in Figure 8b. The influence of NIC on the behavior toward the ORR was confirmed from the polar curves. No change in the onset potential for the oxygen reduction reaction on iron carbide in case of using graphite rode counter electrode

compared to Pt-wire counter electrode. Meanwhile, the activity increases with increasing the rotation speed from 400 to 2500 rpm. The corresponding Koutecky-Levich plot (J^1 vs. $\omega^{-1/2}$) for NIC shows good linearity and the slops are almost the same at a potential ranging from -0.45 to -0.55 V (Figure 8c), indicating the first-order reaction kinetics with respect to the oxygen concentration and constant electron transfer numbers for oxygen reduction reaction at different potentials. The kinetic parameters can be analyzed on the basis of the Koutecky-Levich equations and the transferred electron number (n) was estimated to be 3.73 for the NIC electrode. Moreover, the electron transfer number (n) was further calculated again to be 3.63 from the rotating ring-disk electrode plot (RRDE; Figure 8d). Meanwhile, the corresponding amperometric current (upper curve) for the oxidation of hydrogen peroxide ions (HO_2^-) was also recorded at the Pt ring electrode, which is effective to monitor the formation of intermediate peroxide species. The calculated peroxide yield was 22 % at a potential of 0.5 V *vs.* Ag/AgCl. All the results confirm that our NIC catalyst is responsible for the ORR activity and using Pt-wire or graphitic rode as a counter electrode has no significant effect on the ORR activity.

The dependence of ORR electrocatalytic activity of NIC (Fe_2C) on the specific triple-shelled hollow structure was investigated. We furthermore consider that the retention of the hollow spheres shape during heating is also critical for better ORR catalytic activity.[47] To clarify the shape effect, another control experiment was carried out. Rigorous grinding of NIC catalyst totally destroyed the hollow spheres shape of the sample. We studied its ORR catalytic performance using CV and LSV techniques under the same conditions, as shown in Figure S4. Figure S4a compare the CV curves of NIC catalyst before and after grinding. Figure S4b compares the LSV curves of NIC catalyst before and after grinding. There is a sharp decrease in its ORR catalytic activity after grinding because of the destruction of the hollow spheres shape. It is expected that the hollow spheres shape contributes in the diffusion of oxygen, electrolyte, and intermediate species throughout the whole surface of the material. The catalytic ORR performance of our NIC was further compared with other previously reported materials, as tabulated in **Table 1**. In this comparison we considered the onset potentials value and the number of electron transferred. NIC can be categorized as a four-electron transfer reaction catalyst which is favorable and common for the reduction of O_2. Moreover, the

onset potential is quite lower than some cases even though we have investigated its ORR catalytic activity in diluted alkaline electrolyte (0.1 M KOH).

Conclusion

The solid PB nanocubes with multi-shells were succeefully synthesized. After a subsequent chemical etching, we got the triple-shelled PB hollow spheres with inner cavities. Moreover, multi-shells with micro- and mesopores were observed. We proposed a template free approach which can be applied in the future for the designing and synthesizing hollow spheres with multi-shells and sophisticated nanoarchitecture of any desired inorganic material. After thermal treatments under nitrogen, the triple-shelled PB hollow spheres were converted into orthorhombic iron carbide hollow spheres (Fe_2C). The morphology is well retained even after heating at 450 °C and completely crystallized and collapsed at 700 °C. Such hollow spheres and their derivatives will give us a great opportunity for a new solid state inorganic chemistry and can be applicable in the future for the synthesis of different hybrid metals carbide with fine structures through thermal treatments of PB analogues under nitrogen. The iron carbide hollow spheres realized high electrocatalytic activity and excellent long-term stability towards the ORR, even comparable to the PtC-5% catalyst.

Acknowledgement

The author thanks the Culture Affairs & Missions Sector of the Ministry of Higher Education in Egypt for the financial support.

Notes and references

1 a) S. Wang, L. Wang, T. Yang, X. Liu, J. Zhang, B. Zhu, S. Zhang, W. Huang and S. Wu, *J. Solid State Chem.,* 2010, **183**, 2869–2876, b) L. Xu, J. Xia, K. Wang, L. Wang, H. Li, H. Xu, L. Huang and M. He, *Dalton Trans.*, 2013, **42**, 6468–6477, c) S.-H. Yu, Q.-Z. Yao, G.-T. Zhou and S.-Q. Fu, *ACS Appl. Mater. Interfaces*, 2014, **6**, 10556–10565, d) Q. Li, W. Chen, M. Ju, L. Liu and E. Wang, *J. Solid State Chem*., 2011, **184**, 1373–1380, e) R. Gao, M. Chen, W. Li, S. Zhou and L. Wu, *J. Mater. Chem. A,* 2013, **1**, 2183–2191, f) Y. Li, K. Wang, J. Wu, L. Gu, Z. Lu, X. Wang

and X. Cao, *RSC Adv.,* 2015, **5**, 88277–88286.

2 a) H.-Y. Lian, M. Hu, C.-H. Liu, Y. Yamauchi and K. C.-W. Wu, *Chem. Commun*., 2012, **48**, 5151–5153, b) J. Qi, K. Zhao, G. Li, Y. Gao, H. Zhao, R. Yu and Z. Tang, *Nanoscale*, 2014, **6**, 4072–4077, c) G. Zhang and X. W. Lou (David), *Angew. Chem., Int. Ed.*, 2014, **53**, 9041–9044, d) Z. Zhang, Y. Ji, J. Li, Q. Tan, Z. Zhong and F. Su, *ACS Appl. Mater. Interfaces*, 2015, **7**, 6300–6309, e) J. D. Rocca, D. Liu and W. Lin, *Acc Chem Res.*, 2011, **44**, 957–968.

3 a) M. B. Zakaria, M. Hu, M. Imura, R. R. Salunkhe, N. Umezawa, H. Hamoudi, A. A. Belik and Y. Yamauchi, *Chem. Eur. J*., 2014, **20**, 17375–17384, b) M. B. Zakaria, N. Suzuki, N. L. Torad, M. Matsuura, K. Maekawa, H. Tanabe and Y. Yamauchi, *Eur. J. Inorg. Chem.*, 2013, 2330–2335.

4 a) B.-C. Chen, H.-P. Lin, M.-C. Chao, C.-Y. Mou and C.-Y. Tang, *Adv. Mater*., 2004, **16**, 1657–1661, b) Y. Q. Yeh, H. P. Lin, C. Y. Tang and C. Y. Moua, *J. Colloid Interface Sci.,* 2011, **362**, 354–366.

5 a) J. Hu, M. Chen, X. Fang and L. Wu, *Chem. Soc. Rev*., 2011, **40**, 5472–5491, b) N. Yan, L. Hu, Y. Li, Y. Wang, H. Zhong, X. Hu, X. Kong and Q. Chen, *J. Phys. Chem. C*, 2012, **116**, 7227–7235.

6 S. R. Batten, S. M. Neville and D. R. Turner, *Coordination Polymers: Design, Analysis and Application*; Royal Society of Chemistry, Cambridge, 2009.

7 J. L. C. Rowsell and O. M. Yaghi, *Microporous Mesoporous Mater.*, 2004, **73**, 3–14.

8 J. R. Long and O. M. Yaghi, *Chem. Soc. Rev.,* 2009, **38**, 1213–1214.

9 M. Jacoby, *Chem. Eng. News,* 2008, **86**, 13–16.

10 A. U. Czaja, N. Trukhan and U. Müller, *Chem. Soc. Rev.,* 2009, **38**, 1284–1293.

11 C. Janiak, *Dalton Trans.*, 2003, 2781–2804.

12 H. Furukawa, J. Kim, N. W. Ockwig, M. O'Keeffe and O. M. Yaghi, *J. Am. Chem. Soc.,* 2008, **130**, 11650–11661.

13 H. Furukawa, N. Ko, Y. B. Go, N. Aratani, S. B. Choi, E. Choi, A. Ö. Yazaydin, R. Q. Snurr, M. O'Keeffe, J. Kim and O. M. Yaghi, *Science,* 2010, **329**, 424–428.

14 H. Furukawa and O. M. Yaghi, *J. Am. Chem. Soc.*, 2009, **131**, 8875–8883.

15 H. L. Jiang, Y. Tatsu, Z. H. Lu and Q. Xu, *J. Am. Chem. Soc.*, 2010, **132**, 5586–5587.

16 Y. Q. Lan, H. L. Jiang, S. L. Li and Q. Xu, *Adv. Mater.,* 2011, **23**, 5015–5020.

17 X. Zhao, B. Xiao, A. J. Fletcher, K. M. Thomas, D. Bradshaw and M. J. Rosseinsky, *Science*, 2004, **306**, 1012–1015.

18 S. Bureekaew, S. Shimomura and S. Kitagawa, *Sci. Technol. Adv. Mater.*, 2008, **9**, 014108.

19 J. G. Yu, H. G. Yu, H. T. Guo, M. Li and S. Mann, *Small,* 2008, **4**, 87–91.

20 H. Han, S. Zhang, H. Hou, Y. Fan and Y. Zhu, *Eur. J. Inorg. Chem.*, 2006, 1594–1600.

21 S. Jurisson, D. Berning, W. Jia and O. Ma, *Chem. Rev.*, 1993, **93**, 1137–1156.

22 A.-C. Albertsson and I. K. Varma, *Biomacromolecules*, 2003, **4**, 1466–1486.

23 P. J. Sadler, H. Li and H. Sun, *Coord. Chem. Rev.*, 1999, **185–186**, 689–709.

24 F. Cheng, H. Ma, Y. Li and J. Chen, *Inorg. Chem.*, 2007, **46**, 788–794.

25 K. Seki and W. Mori, *J. Phys. Chem. B,* 2002, **106**, 1380–1385.

26 X. Lai, J. E. Halperta and D. Wang, *Energy Environ. Sci.,* 2012, **5**, 5604–5618.

27 G. Liang, J. Xu and X. Wang, *J. Am. Chem. Soc*., 2009, **131**, 5378–5379.

28 X. Zhang, M. A. Ballem, M. Ahrén, A. Suska, P. Bergman and K. Uvdal, *J. Am. Chem. Soc.*, 2010, **132**, 10391–10397.

29 R. Ameloot, F. Vermoortele, W. Vanhove, M. B. J. Roeffaers, B. F. Sels and D. E. D. Vos, *Nat. Chem.,* 2011, **3**, 382–387.

30 a) M. Hu, S. Furukawa, R. Ohtani, H. Sukegawa, Y. Nemot, J. Reboul, S. Kitagawa and Y. Yamauchi, *Angew. Chem. Int. Ed.*, 2012, **51**, 984–988, b) L. Cao, Y. Liu, B. Zhang and L. Lu, *ACS Appl. Mater. Interfaces,* 2010, **2**, 2339–2346.

31 J. Huo, L. Wang, E. Irran, H. Yu, J. Gao, D. Fan, B. Li, J. Wang, W. Ding, A. M. Amin, C. Li and L. Ma, *Angew. Chem. Int. Ed.*, 2010, **49**, 9237–9241.

32 H. J. Lee, W. Cho and M. Oh, *Chem. Commun.,* 2012, **48**, 221–223.

33 R. McHale, N. Ghasdian, Y. Liu, M. B. Ward, N. S. Hondow, H. Wang, Y. Miao, R. Brydson and X. Wang, *Chem. Commun.*, 2010, **46**, 4574−4576.

34 S. Bao, W. Qin, Q. Wu, G. Liang, F. Zhua and Q. Wu, *Dalton Trans.,* 2013, 42, 5242–5246.

35 a) M. B. Zakaria, M. Hu, N. Hayashi, Y. Tsujimoto, S. Ishihara, M. Imura, N. Suzuki, Y.-Y. Huang, Y. Sakka, K. Ariga, K. C.-W. Wu and Y. Yamauchi, *Eur. J. Inorg. Chem.*, 2014, 1137–1141, b) M. B. Zakaria, A. A. Belik, H.-Y. Hsieh, Y.-T.

Liao, Y. Yamauchi and K. C.-W. Wu, *Chem. Asian J.*, 2015, **10**, 1457–1462.

36 a) J. G. Cosgrove, R. L. Collins, D. S. Murty, *J. Am. Chem. Soc.*, 1973, **95**, 1083–1086, b) P. K. Gallagher and B. Prescott, *Inorg. Chem.*, 1970, **9**, 2510–2512, c) J. F. Allen and A. K. Bonnette, *J. Inorg. Nucl. Chem.,* 1974, **36**, 1011–1016, d) H. Inoue, T. Nakazawa, T. Mitsuhashi, T. Shirai and E. Fluck, *Hyperfine Interact.,* 1989, ***46***, 725–731.

37 M. Hu, A. A. Belik, M. Imura and Y. Yamauchi, *J. Am. Chem. Soc.,* 2013, **135**, 384–391

38 H. Ming, N. L. K. Torad, Y.-D. Chiang, K. C.-W. Wu and Y. Yamauchi, *CrystEngComm*., 2012, **14**, 3387–3396.

39 C. Aparicio, L. Machala and Z. Marusak, *J. Therm. Anal. Calorim.*, 2012, **110**, 661–669.

40 X.-Q. Zhang, S.-W. Gong, Y. Zhang, T. Yang, C.-Y. Wang and N. Gu, *J. Mater. Chem.*, 2010, **20**, 5110–5116.

41 a) A. G. El-Deen, N. A. M. Barakat, K. A. Khalil and H. Y. Kim, *New J. Chem.,* 2014, **38**, 198–205, b) W. Zuo, C. Wang, Y. Li and J. Liu, *Sci. Rep*., 2014, **5**, 7780.

42 J. H. Shim, J. Kim, C. lee and Y. Lee, *Chem. Mater.,* 2011, **23**, 4694–4700.

43 a) Y. Xiao, C. Hu, L. Qu, C. Hu and M. Cao, *Chem. Eur. J.,* 2013, **19**, 14271–14278, b) W. Hu, Y. Wang, X. Hu, Y. Zhou and S. Chen, *J. Mater. Chem.,* 2012, **22**, 6010–6016.

44 a) Z.-S. Wu, S. Yang, Y. Sun, K. Parves, X. Feng and K. Müllen, *J. Am. Chem. Soc.*, 2012, **134**, 9082–9085, b) M. S. El-Deab and T. Ohsaka, *Angew. Chem. Int. Ed.*, 2006, **45**, 5963–5966, c) L. Demarconnay, C. Coutanceau and J.-M. Léger, *Electrochimica. Acta*, 2009, **49**, 4513–4521.

45 a) J. Tang, J. Liu, C. Li, Y. Li, M. O. Tade, S. Dai and Y. Yamauchi, *Angew. Chem. Int. Ed.*, 2015, **54**, 588–593, b) J. Masa, C. Batchelor-McAuley, W. Schuhmann and R. G. Compton, *Nano Research*, 2014, **7**, 71–78, c) L. Zhang, K. Lee and J. Zhang, *Electrochimica. Acta,* 2007, **52**, 3088–3094.

46 a) H. Dong, R. Feng, X. Ai, Y. Cao, H. Yang and C. Cha, *J. Phys. Chem. B,* 2005, **109**, 10896–10901, b) A. M. Meléndez, E. Lima and I. González, *J. Phys. Chem. C*, 2008, **112**, 17206–17213.

47 M. B. Zakaria, M. Hu, M. Pramanik, C. Li, J. Tang, A. Aldalbahi, S. M. Alshehri, V.

Malgras and Y. Yamauchi, *Chem. Asian J.,* 2015, **10**,1541–1545.

48 Y. Tan, C. Xu, G. Chen, X. Fang, N. Zheng and Q. Xie, *Adv. Funct. Mater.,* 2012, **22**, 4584–4591.

49 D. Singh, Juan Tian, K. Mamtani, J. King, J. T. Miller and U. S. Ozkan, *J. Catal.,* 2014, **317**, 30–43.

50 Y. Liang, Y. Li, H. Wang, J. Zhou, J. Wang, T. Regier and H. Dai, *Nat. Mater.,* 2011, **10**, 780–786.

51 F. Cheng, J. Shen, B. Peng, Y. Pan, Z. Tao and J. Chen, *Nat. Chem.*, 2011, **3**, 79–84.

52 L. Gu, L. Jiang, J. Jin, J. Liu and G. Sun, *Carbon*, 2015, **82**, 572–578.

53 J. Zhang, D. He, H. Su, X. Chen, M. Pan and S. Mu, *J. Mater. Chem. A,* 2014, **2**, 1242–1246.

54 J. Zhang, A. Byeon and J. W. Lee, Chem. Commun., 2014, 50, 6349–6352.

55 A. Garsuch, R. Yang, A. Bonakdarpour and J. R. Dahn, Electrochimica. Acta, 2008, 53, 2423–2429.

Figures and figure captions

Figure 1

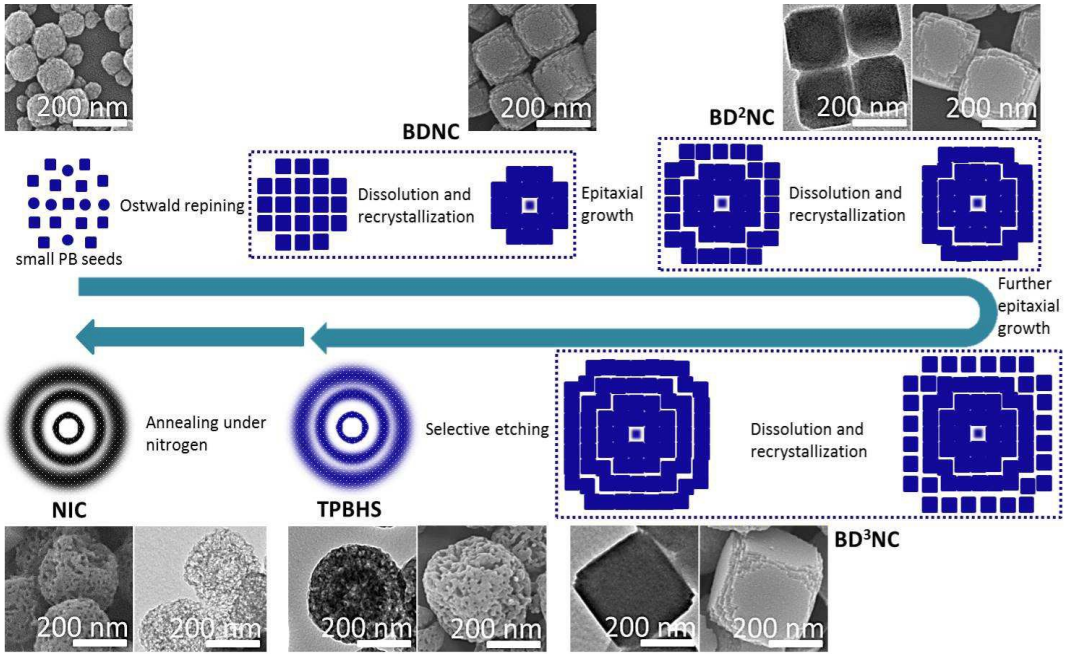

Figure 1 Schematic illustration of the synthetic pathway of TPBHS and its thermal conversion into NIC with retention of the original morphology.

Figure 2

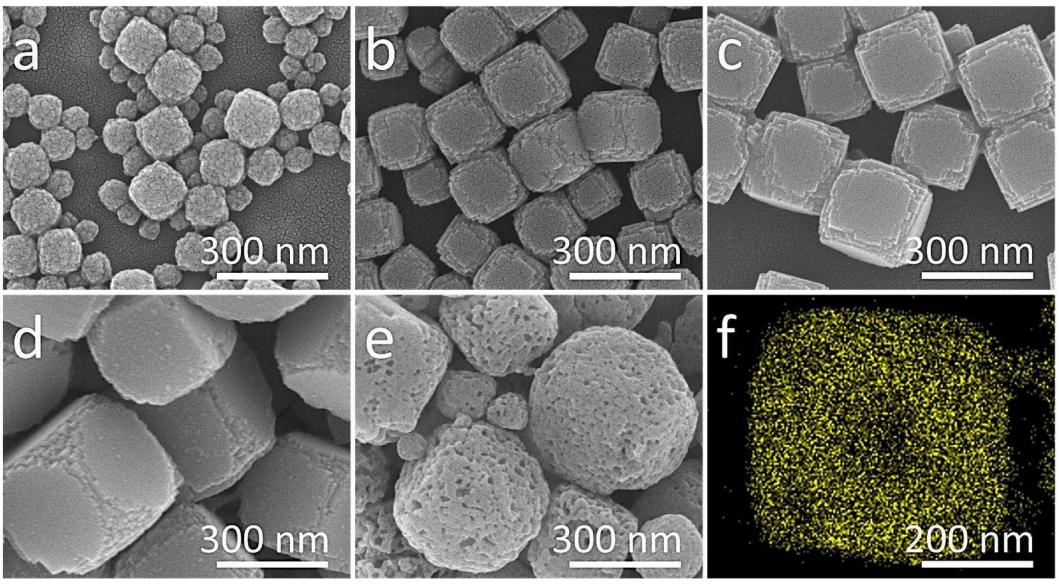

Figure 2 SEM images of a) the small PB seeds, b) BDNC, c) BD^2NC, d) BD^3NC, and e) TPBHS and f) elemental mapping of Fe atoms on the top surface of TPBHS.

Figure 3

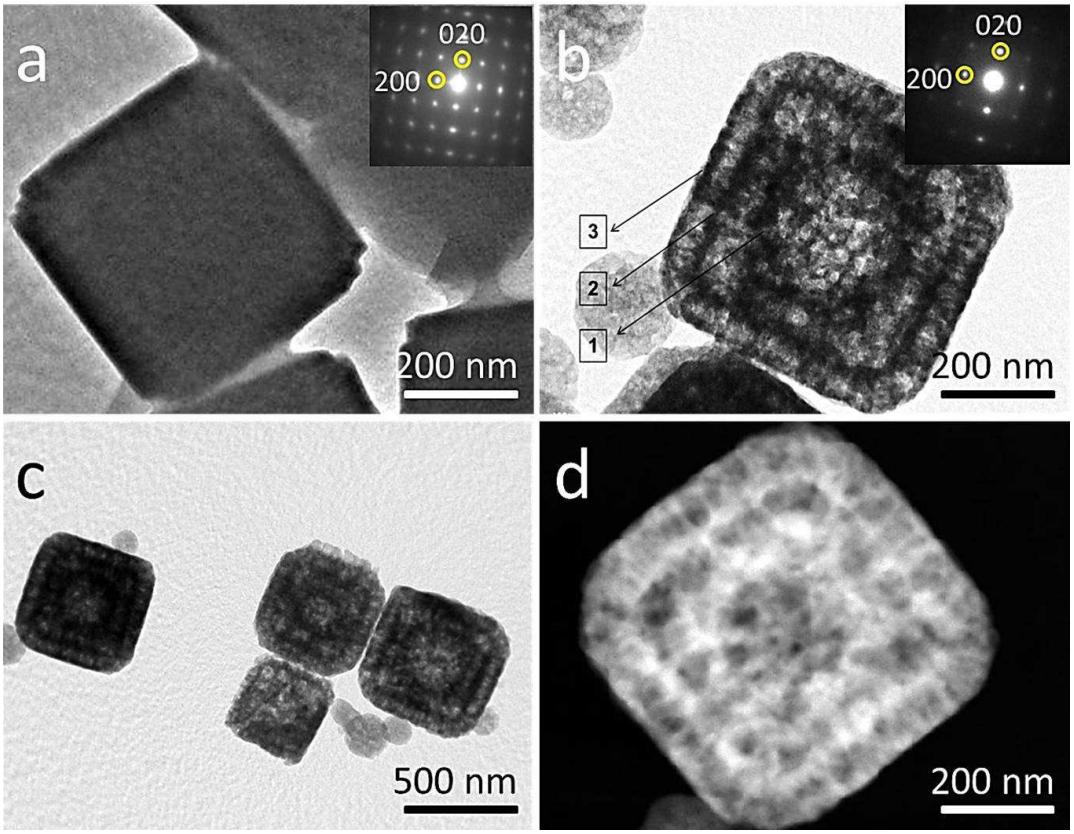

Figure 3 a,b) High magnification TEM images of selected particle of BD^3NC and TPBHS, respectively, insets are the corresponding ED images. c,d) Low magnification TEM and HAADF-STEM images of TPBHS, respectively.

Figure 4

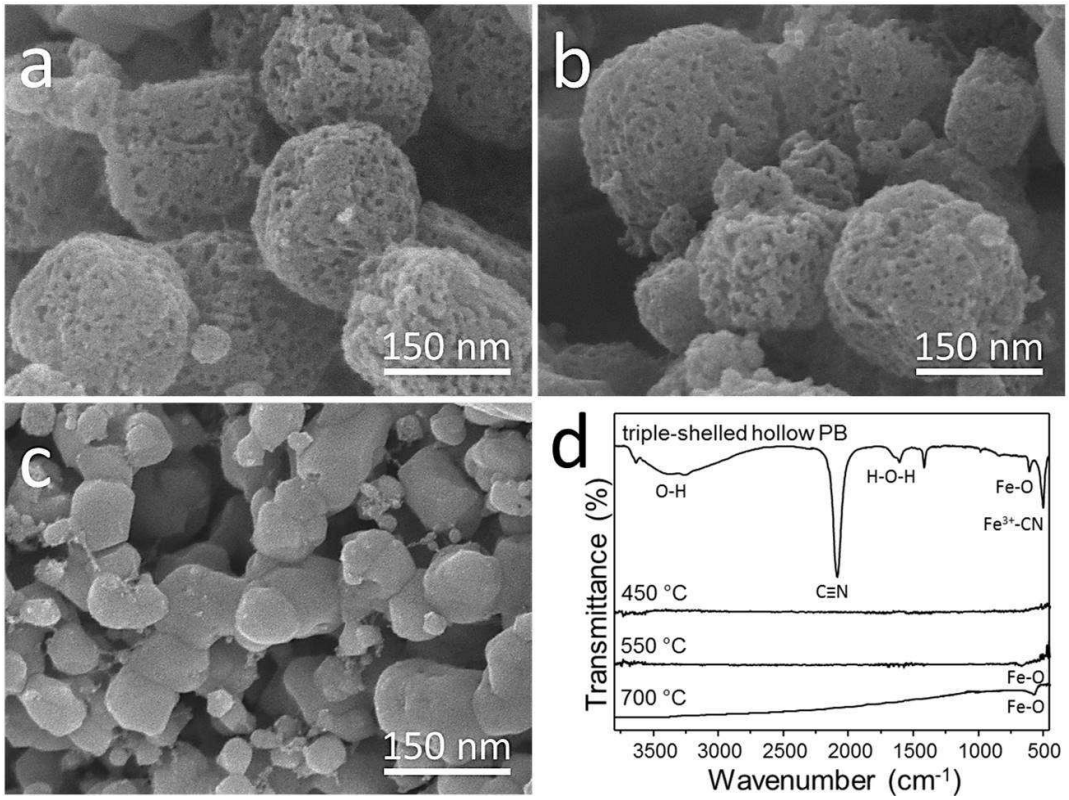

Figure 4 SEM images of NIC obtained after calcining TPBHS under nitrogen at a) 450 ℃, b) 550 ℃, and c) 700 ℃ for 1h and d) their corresponding FTIR spectra.

Figure 5

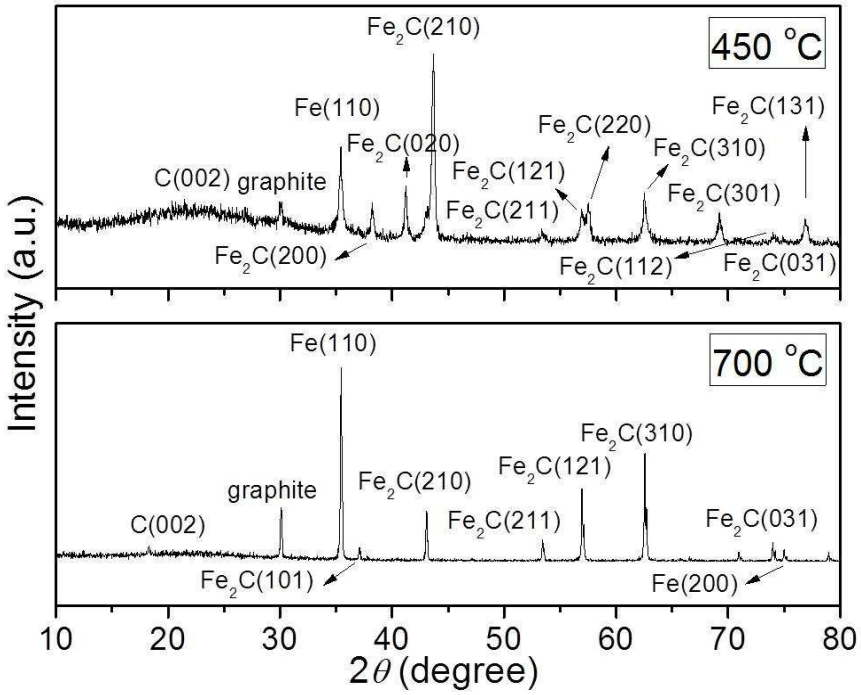

Figure 5 Wide-angle XRD patterns of NIC obtained after calcination of TPBHS under nitrogen at a) 450 ℃ and b) 700 ℃ for 1h.

Figure 6

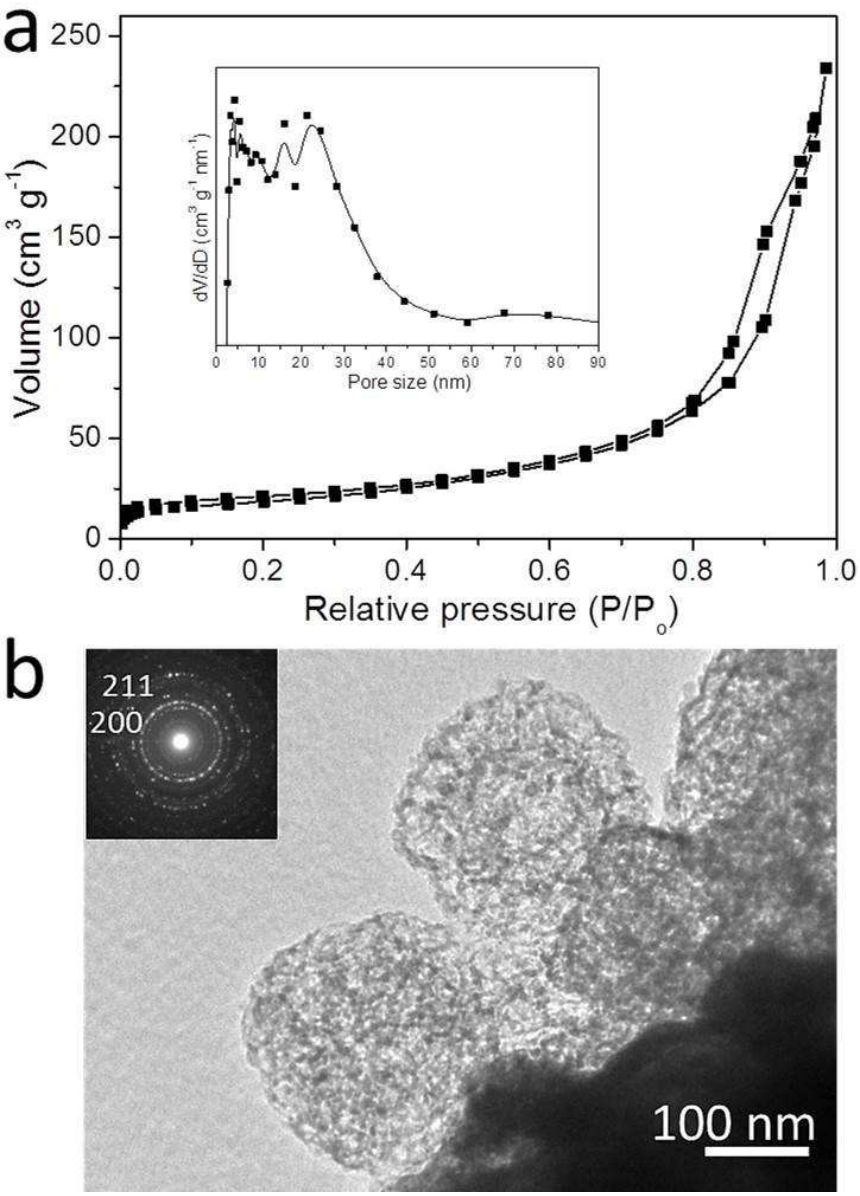

Figure 6 a) Nitrogen gas adsorption-desorption isotherms (inset is the pore size distribution curve) and b) TEM image (inset is the ED image of selected particle) of NIC obtained after calcination at 450 °C for 1h.

Figure 7

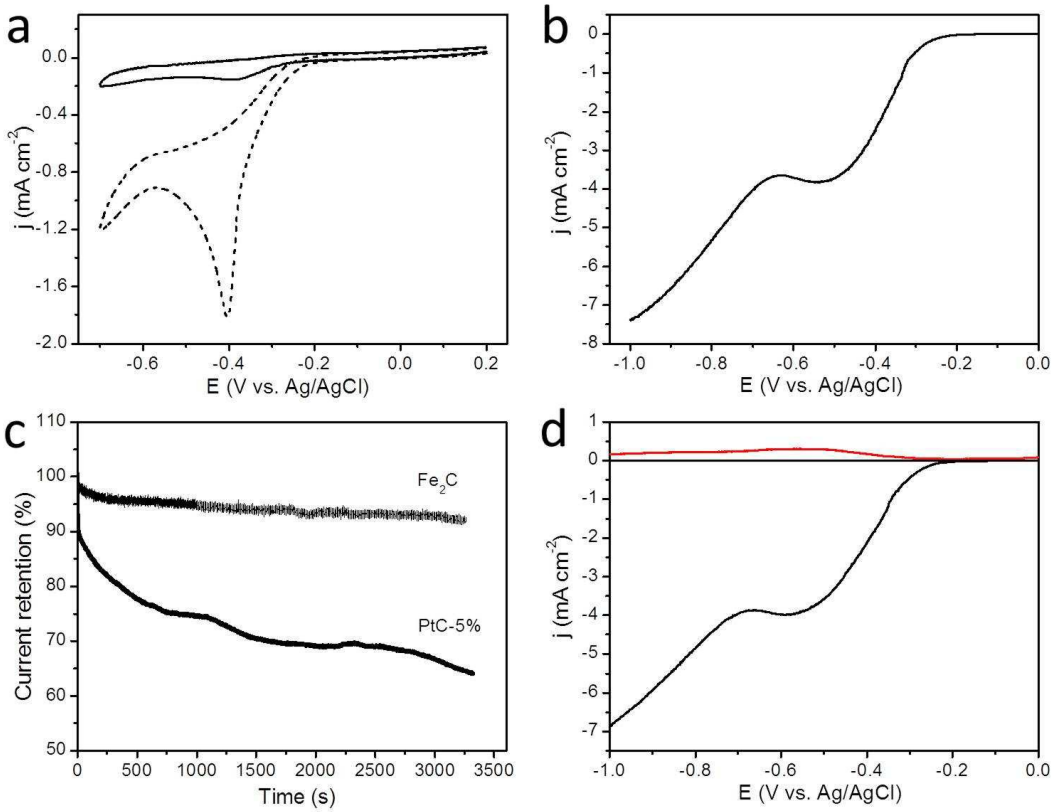

Figure 7 a) Cyclic voltammetric (CV) curves obtained under (solid line) N_2- and (dashed line) O_2-saturated 0.1 M KOH solutions catalyzed by NIC. b) ORR polarization curves of the rotating desk electrode (RDE) modified with NIC in an O_2-saturated 0.1 M KOH solution at a rotation rate of 1600 rpm and a scan rate of 10 mV s^{-1}. c) The current retention plot during chronoamperometric measurements of NIC and commercial PtC-5% for 3500 s at a constant potential of -0.5 V. d) Rotating ring-disk electrode (RRDE) test of the ORR on NIC in an O_2-saturated 0.1 M KOH electrolyte at a scan rate of 10 mV s^{-1}. The rotation rate was 1600 rpm and the Pt ring electrode is poised at 0.5 V for oxidizing HO_2^- intermediate. These measurements were carried out using Pt-wire as a counter electrode.

Figure 8

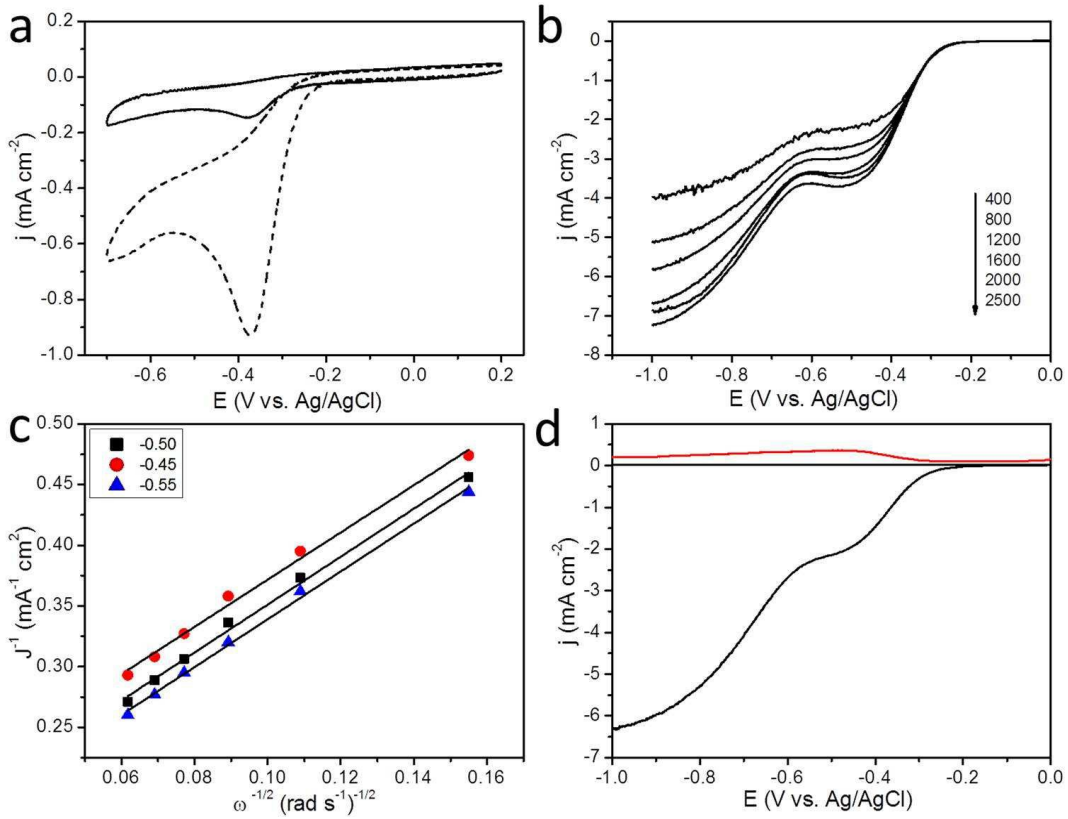

Figure 8 a) Cyclic voltammetric (CV) curves obtained under (solid line) N_2- and (dashed line) O_2-saturated 0.1 M KOH solutions catalyzed by NIC. b) Polarization curves of NIC at different rotation rates in O_2-saturated 0.1 M KOH solutions with a scan rate of 10 mV s^{-1} and c) the corresponding Koutrcky-Levich plot of J^{-1} *vs.* $\omega^{-1/2}$ at different potentials. d) RRDE test of the ORR on NIC in an O_2-saturated 0.1 M KOH electrolyte at a scan rate of 10 mV s^{-1}. The rotation rate was 1600 rpm and the Pt ring electrode is poised at 0.5 V for oxidizing HO_2^- intermediate. These measurements were carried out using graphite rode as a counter electrode.

Table 1 Comparison between the electrocatalytic activity toward ORR of our catalyst (Fe_2C) and other previously reported materials. *n* is the number of electron transferred during the ORR.

Sample information	Electrolyte	Onset potential (mV *vs.* Ag/AgCl)	*n*	References
Fe_2C	0.1 M KOH	-200	3.7	Present work
Mesoporous N-doped carbon	0.1 M KOH	-230	2.6	48
N-containing carbon/CNx	0.5 M H_2SO_4	-245	2.4	49
N-coordinated iron–carbon/FeNC	0.5 M H_2SO_4	-155	3.8	49
N-doped graphene	0.1M KOH	-160	2.7	50
$CoMn_2O_4$	0.1 M KOH	-180	2.9	51
Calcined iron carbide/N-doped carbon	0.1 M NaOH	-160	3.0	52
Calcined N-doped carbon	0.1 M NaOH	-260	2.0	52
FeNxC/C–S	0.1 M $HClO_4$	-115	3.9	53
Boron-doped carbon–iron/ FeBC105	1.0 M NaOH	-140	2.0	54
Boron-doped carbon–iron/ FeBC085	1.0 M NaOH	-150	2.0	54
Boron-doped carbon–iron/ FeBC050	1.0 M NaOH	-220	2.0	54
Co-C-N-B/low boron content	0.1 M $HClO_4$	-400	----	55
Co-C-N-B/high boron content	0.1 M $HClO_4$	-315	----	55
Fe-C-N-B/ low boron content	0.1 M $HClO_4$	-470	----	55
Fe-C-N-B/high boron content	0.1 M $HClO_4$	-315	----	55

Graphical abstract

A controlled thermal treatment of the triple-shelled hollow Prussian blue spheres yielded well-retained nanoporous iron carbide for efficient electrocatalytic ORR.